

# Confinement-induced motion of ciliates

G. C. Antunes<sup>1,\*</sup> and H. Stark<sup>1</sup>

<sup>1</sup>*Institute of Physics and Astronomy, Division of Theoretical Physics,  
Technische Universität Berlin, Hardenbergstrasse 36, 10623, Berlin, Germany*  
(Dated: January 19, 2026)

The time dynamics of flagellar and ciliary beating is often neglected in theories of microswimmers, with the most common models prescribing a time-constant actuation of the surrounding fluid. By explicitly introducing a metachronal wave, coarse-grained to a sinusoidal surface slip velocity, we show that a spatial resonance between the metachronal wave and the corrugation of a confining cylindrical channel enables a ciliate to swim even when it cannot move forward in a bulk fluid. Using lubrication theory, we reduce the problem to the Adler equation that reveals an oscillatory and ballistic swimming regime. Interestingly, a ciliate can even reverse its swimming direction in a corrugated channel compared to the bulk fluid.

It is widely known that bodies undergoing a reciprocal motion cannot propel in bulk fluids at low Reynolds numbers [1]. Thus, microorganisms need to rely on structures such as flagella [2] or cilia [3] which beat in a non-reciprocal fashion [1, 4]. Due to the challenge of fully capturing the dynamics of each flagellum or cilium, theoretical descriptions of microswimmers typically rely on a coarse-graining. Examples include the specification of an effective surface slip velocity in the well-known squirmer model [5–9] or a truncated multipolar expansion for the swimmer-generated flow fields [7, 10–13]. Most of the theoretical work focuses on the time-averaged actuation of the fluid by the flagellar or ciliary beat, *i.e.*, prescribes slip velocity profiles and multipolar expansion coefficients that are constant in time. While such descriptions may capture the dynamics of microswimming on long timescales, they fail to describe the dynamics on the timescale of the beating period [14–16]. In this Letter, we show that accounting for the time dynamics of ciliary beating is crucial to understanding the motion of ciliates in spatially inhomogeneous confinement.

To do so, we use both lattice-Boltzmann simulations and a theoretical analysis based on the lubrication approximation. The latter is a versatile tool and has been used extensively in different contexts such as biological flows [17–20], fluid-mediated interactions [21–24], chemically-active [25–29] or charged [30, 31] flows, as well as droplets and films [32–35].

In the following, we demonstrate how a sinusoidal metachronal wave coarse-grained to a surface slip velocity that spatially resonates with the corrugation of a confining channel enables ciliates to swim, even when they cannot move forward in a bulk fluid. In particular, we reduce the swimming dynamics to the Adler equation that shows an oscillatory and ballistic regime.

Specifically, we aim to investigate the motion of a ciliate in a cylindrical channel aligned with the  $x$  axis and whose local radius  $R(x)$  varies according to

$$R(x) = R_c + R_0 + R_1 \cos(k_w x). \quad (1)$$

\* g.antunes@tu-berlin.de

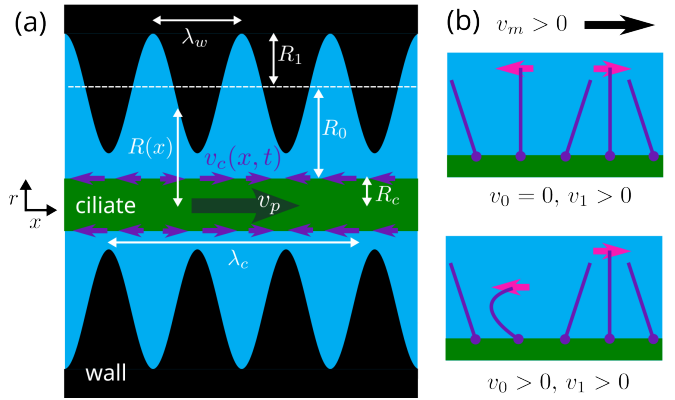


FIG. 1. (a) Schematic of a long ciliate (green cylinder) that swims in a cylindrical channel with corrugated walls, which are depicted in black while the surrounding fluid is drawn in blue. The cilia are coarse-grained to an effective slip velocity  $v_c$ , represented by purple arrows on the surface of the ciliate, while the ciliate moves with velocity  $v_p$ . (b) Schematics of a reciprocal (above) and non-reciprocal (below) ciliary beat pattern. Pink arrows indicate the direction of motion of the single cilia. The metachronal wave travels from left to right with speed  $v_m > 0$ . For a sufficiently sparse ciliary carpet, the net fluid flow of the reciprocal beat pattern is negligible.

Here,  $R_c$  is the radius of the ciliate,  $R_0$  is the spatially averaged distance between the ciliate and the channel wall,  $R_1$  is the amplitude of the corrugation, and  $k_w$  is its wavenumber [see Fig. 1 (a)]. The ciliate is modeled as a cylinder whose length  $L_c$  is much larger than the wavelength  $\lambda_w = 2\pi/k_w$  and so can be considered effectively infinite in length. Ciliates are covered by a carpet of beating cilia, which move fluid along the ciliate surface and thereby propel the microorganism forward. Because variations in height of the ciliary layer are typically much smaller than  $R_c$  [36], we coarse-grain the operation of this layer into an effective slip velocity tangential to the surface of the ciliate,

$$\mathbf{v}(x, r = R_c, t) = [v_p(t) + v_c(x, t)]\mathbf{e}_x, \quad (2)$$

Here,  $\mathbf{v}(x, r, t)$  is the velocity of the fluid constrained between the ciliate and the corrugated channel wall,  $v_p(t)$

is the swimming velocity of the ciliate, which needs to be determined, and the slip velocity  $v_c(x, t)$  encodes the ciliary beating. Contrary to previous work, we do not take the velocity  $v_c(x, t)$  to be constant in time, as we aim to capture the time-varying actuation by the ciliary layer and its effect on the surrounding fluid. Indeed, cilia beat in a periodic fashion with period  $T_c$  and their motions often split into a power and recovery stroke [3, 37] [see Fig. 1(b)] that are non-reciprocal, enabling net swimming and motion of fluid.

Typically, neighboring cilia beat with a phase lag and thereby form a metachronal wave [38–41] with a wavelength  $\lambda_c$  much smaller than the size  $L_c$  of the ciliate [36]. To capture these features, we propose for the slip velocity at the surface of the ciliate,

$$v_c(x, t) = v_0 + v_1 \cos\{k_c[x - x_p(t)] - \omega t\}, \quad (3)$$

where  $v_0$  is the time-averaged velocity imposed by the ciliary layer, and  $v_1$  is the amplitude of the metachronal wave. Here,  $v_0 \neq 0$  indicates that the ciliary carpet induces a net fluid transport across the surface of the ciliate. Such a transport may result from non-reciprocal power and recovery strokes or even from reciprocally beating cilia that are packed densely enough so that hydrodynamic interactions lead to net fluid flow [42]. Furthermore,  $k_c = 2\pi/\lambda_c$  is the wavenumber of the metachronal wave and  $\omega = 2\pi/T_c$  is the ciliary frequency. As a result, the metachronal wave travels with a speed  $v_m = \omega/k_c$  in the body-fixed frame of the ciliate. The origin of this frame of reference moves with velocity  $v_p(t)$  along the  $x$  direction and is located at position  $x_p(t) = \int_0^t v_p(t') dt'$ .

Now, the main task is to determine the swimming velocity of the ciliate,  $v_p(t)$ . At low Reynolds numbers, the fluid obeys Stokes' equations and the incompressibility condition,  $\nabla P(\mathbf{r}, t) = \mu \Delta \mathbf{v}(\mathbf{r}, t)$  and  $\nabla \cdot \mathbf{v}(\mathbf{r}, t) = 0$ , where  $\mu$  is the dynamic viscosity and  $P(\mathbf{r}, t)$  is the pressure. No-slip boundary conditions apply at the surface of the channel,  $\mathbf{v}(x, r = R(x), t) = 0$ . The ciliate swims in an otherwise quiescent fluid such that no external pressure gradient is applied, and moves force-free meaning without an applied external force,  $\oint_S \boldsymbol{\sigma}(\mathbf{r}, t) \cdot \mathbf{n}(\mathbf{r}, t) dS = \mathbf{0}$ , where  $S$  is the surface of the ciliate,  $\boldsymbol{\sigma}(\mathbf{r}, t)$  is the Newtonian stress tensor,  $\boldsymbol{\sigma}(\mathbf{r}, t) = -P(\mathbf{r}, t) \mathbf{I} + \mu [\nabla \otimes \mathbf{v}(\mathbf{r}, t) + (\nabla \otimes \mathbf{v})^T(\mathbf{r}, t)]$ , and  $\mathbf{n}(\mathbf{r}, t)$  is the outer normal.

*Lubrication theory and linearization.* We solve the above equations by employing the lubrication approximation [43], whereby the velocity field is taken to vary much more rapidly in the radial direction than in the  $x$  direction. Such an assumption is true if the characteristic lengths in the radial direction ( $R_0, R_1$ ) are much smaller than the characteristic lengths along the  $x$  axis ( $\lambda_w, \lambda_c$ ). Ultimately, we arrive at the following equation for the time evolution of  $x_p(t)$ ,

$$\dot{x}_p(t) = -\langle \mathcal{G}(x) v_c(x, t) \rangle, \quad (4)$$

where the angle brackets indicate an average over  $x$ , and the local mobility coefficient  $\mathcal{G}(x)$  only depends on the

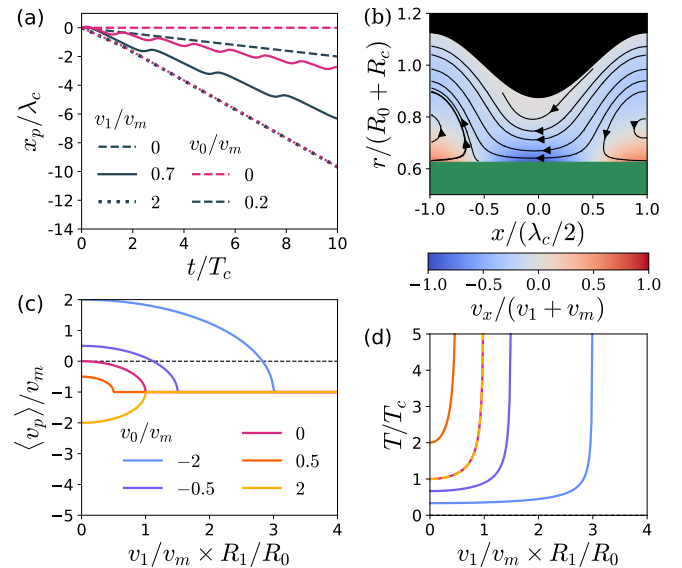


FIG. 2. (a) Position  $x_p$  of the ciliate plotted *vs.* time for different values of  $v_0/v_m$  and  $v_1/v_m$ . (b) Snapshot of the fluid flow for  $v_0 = 0$ ,  $R_0/R_c = 3/5$ ,  $R_1/R_0 = 1/3$ ,  $R_0/\lambda_c = 3/20$ ,  $v_1/v_m = 3.6$ , taken at  $t/T_c = 3.78$ . The fluid streamlines are shown in black and the color indicates the flow-velocity component  $v_x$ . In this moment, the ciliate moves to the left. (c) Time-averaged ciliate velocity  $\langle v_p \rangle$  and (d) period of oscillatory motion  $T$  plotted *vs.* the amplitude of ciliary slip velocity,  $v_1/v_m$ , times the amplitude of channel corrugation,  $R_1/R_0$ , for several values of  $v_0/v_m$ . In all panels  $\lambda_c = \lambda_w$ .

shape of the channel wall and the radius of the ciliate (see Supplementary Material in Sect. I). In particular,  $\langle \mathcal{G}(x) \rangle = 1$ . Since  $v_c(x, t)$  is a sinusoid [Eq. (3)], one immediately obtains

$$\dot{x}_p(t) = \begin{cases} -v_0 - v_1 \frac{\mathcal{G}_n}{2} \cos[k_c x_p(t) + \omega t] & \text{if } \lambda_c = \lambda_w/n \\ -v_0 & \text{if } \lambda_c \neq \lambda_w/n, \end{cases} \quad (5)$$

where  $n$  is a natural number and  $\mathcal{G}_n$  are the respective Fourier coefficients of  $\mathcal{G}(x)$ . In the limits of small curvature of the ciliate body ( $R_0/R_c \ll 1$ ) and shallow corrugation ( $R_1/R_0 \ll 1$ ), a linearization with respect to these parameters shows that only the Fourier coefficient for  $n = 1$  is non-zero, becoming  $\mathcal{G}_1 = 2R_1/R_0$ . Clearly, in the case where the spatiotemporal dynamics of the ciliary carpet is discarded ( $v_1 = 0$ ), the channel is flat ( $R_1 = 0$ ), or the wavelengths of the metachronal wave and the corrugation do not match ( $\lambda_c \neq \lambda_w/n$ ), the ciliate swims with a velocity  $v_p = -v_0$ , as it would when placed in bulk fluid. However, if none of the three previous conditions are met, a resonance between the local hydrodynamic resistance (resulting from the corrugated wall profile) and the fluid forcing (resulting from the metachronal wave) generates the extra term in Eq. (5). The effect on the trajectory of the ciliate can be seen by numerically solving Eq. (5), the results of which we show in Fig. 2(a). When  $v_1/v_m = 0.7$  (full lines), where  $v_m$  is the metachronal-

wave speed, the ciliate swims with an overall drift and superimposed oscillations.

Remarkably, such a drift occurs even when the ciliary carpet does not generate net fluid transport along its surface [ $v_0 = 0$ , magenta lines in Fig. 2(a)]. An organism with  $v_0 = 0$  cannot propel itself in a bulk fluid, but it is able to when placed in a corrugated channel of appropriate wavelength. The cause is an imbalance between the net propulsion generated by the power stroke and the recovery stroke. While both generate the same slip velocity (in magnitude), they are performed in regions of different film thickness, where the generated flow experiences different effective hydrodynamic resistances [see Fig. 2(b)]. The result is directed motion even when the time-and-space-averaged slip velocity is zero. Depending on the phase difference between the corrugated wall and the velocity profile on the surface of the ciliate, the ciliate swims either with or against the metachronal wave. What enables net propulsion (rather than oscillation about a certain position) is the fact that the metachronal wave has a given direction. Because the velocity of the metachronal wave in the laboratory frame is the sum of the velocities of the ciliate velocity and of the metachronal wave, configurations of the flow leading to swimming against the wave persist longer than configurations which lead to swimming with the wave. As such, the ciliate spends more time swimming against the metachronal wave than with it, as can be seen in Supplementary Video 1.

For high enough values of  $v_1$ , the trajectory is no longer oscillatory, but instead becomes ballistic, in the direction opposite to the metachronal wave, and exactly at its speed [see Fig. 2 (a)]. Thus, no matter how strongly the ciliary carpet may push, the ciliate is constrained to swim with the metachronal phase speed  $v_m$ . In this regime, the slip velocity profile becomes stationary in the laboratory frame of reference, as can be seen in Supplementary Video 2. Thus, the phase difference between the channel corrugation and the slip velocity profile is constant, and no further acceleration is possible.

One can indeed rationalize the two observed dynamical regimes by introducing the non-dimensional coordinate in the frame of reference moving with the metachronal wave,  $\xi = k_c x_p(t) + \omega t + \pi/2$ . Rescaling time by  $\omega^{-1}$ , Eq. (5) for  $\lambda_c = \lambda_w/n$  can be cast in the form of the well-known Adler equation [44–46],

$$\dot{\xi} = a - b \sin \xi \quad \text{with } a = 1 - \frac{v_0}{v_m} \quad \text{and } b = \frac{v_1}{v_m} \frac{\mathcal{G}_n}{2}, \quad (6)$$

which indeed shows a dynamical transition for

$$\left| \frac{a}{b} \right| = \left| \left( 1 - \frac{v_0}{v_m} \right) / \left( \frac{v_1}{v_m} \frac{\mathcal{G}_n}{2} \right) \right| = 1. \quad (7)$$

It is now possible to infer the time-averaged velocity of the ciliate,  $\langle v_p \rangle$  [44, 46]. In the phase-locked regime ( $|a/b| < 1$ ), one obtains  $\langle v_p \rangle = -v_m$ , while the oscillatory regime ( $|a/b| > 1$ ) yields

$$\frac{\langle v_p \rangle}{v_m} = \left( 1 - \frac{v_0}{v_m} \right) \sqrt{1 - \left( \frac{\frac{v_1}{v_m} \frac{\mathcal{G}_n}{2}}{1 - \frac{v_0}{v_m}} \right)^2} - 1. \quad (8)$$

As mentioned earlier, in the linearized limit,  $\mathcal{G}_n = 2R_1/R_0 \delta_{1n}$ , where  $\delta_{ij}$  is the Kronecker symbol. So, in Fig. 2 (c), we plot the time-averaged ciliate velocity *versus*  $v_1/v_m \times R_1/R_0$  for different  $v_0/v_m$  and  $\lambda_c = \lambda_w$ . For increasing  $v_1 R_1$ , the ciliate velocity approaches that of the metachronal wave. Depending on  $v_0$ ,  $\langle v_p \rangle$  either decreases or increases towards  $-v_m$ . In fact, the ciliate even reverses direction with respect to the bulk fluid if  $v_0/v_m < 0$  and  $v_1/v_m \times R_1/R_0 > \sqrt{a^2 - 1}$ . Thus, an antiplectic ciliate, which swims in the same direction as the metachronal wave in the bulk fluid (*e.g.* *Paramecium* [47]), may become a symplectic swimmer, which moves opposite to the metachronal wave (*e.g.* *Opalina* [48]) in a sufficiently corrugated channel.

The period of the oscillatory motion,  $T$ , can also be obtained analytically [44, 46],

$$T = \frac{T_c}{\sqrt{\left( \frac{v_0}{v_m} - 1 \right)^2 - \left( \frac{v_1}{v_m} \frac{\mathcal{G}_n}{2} \right)^2}}. \quad (9)$$

It diverges at the transition from the oscillatory to the phase-locked regime, and takes values both below and above  $T_c$ , as shown in Fig. 2(d).

*Full lubrication theory and lattice-Boltzmann simulations.* In the full theory, the Fourier coefficients  $\mathcal{G}_n$ , and thereby  $\langle v_p \rangle$ , have a non-trivial dependence on  $R_1$  and  $R_c$ , which we now explore. We also support our findings with lattice-Boltzmann simulations [49]. In the following, we shall focus on the motion of ciliates with  $v_0 = 0$  since this case provides the clearest and physically most interesting manifestation of the interplay between corrugation and slip velocity.

First, in Fig. 3(a) we again observe the expected transition from the oscillatory to the phase-locked regime with  $\langle v_p \rangle = -v_m$  for increasing wave amplitude  $v_1$ . As deduced from Eq. (8), all curves collapse on a master curve of the form  $\langle v_p \rangle/v_m = \sqrt{1 - v_1^2/v_*^2} - 1$  with the critical wave amplitude  $v_* = 2v_m/\mathcal{G}_1$  separating the two dynamical regimes from each other [see inset of Fig. 3(a)]. In Fig. 3(b), the swimming velocity shows two local maxima for increasing corrugation  $R_1/R_0$ . The maximum at  $R_1/R_0 \approx 1$  corresponds to the limiting case where fluid transport through the bottlenecks and along the entire ciliate is greatly suppressed such that the velocity field instead resembles an array of vortices. Swimming in such a channel geometry is not due to fluid transport from fore to aft, but due to an effective grip between the ciliate and the channel wall mediated by the enclosed pockets of fluid. Surprisingly, between the two local maxima, a strong dip in  $|\langle v_p \rangle|$  occurs at  $R_1^*/R_0$ , the value of which is mainly determined by  $R_0/R_c$ . In fact, the instantaneous ciliate velocity becomes zero as well due to a root

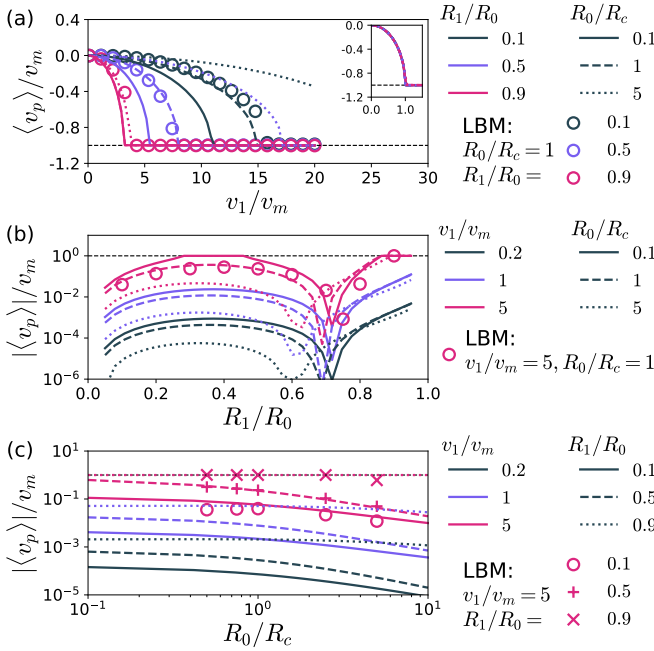


FIG. 3. Time-averaged ciliate velocity  $\langle v_p \rangle$  as function of (a) ciliary wave amplitude  $v_1/v_m$ , (b) corrugation amplitude  $R_1/R_0$ , and (c) ciliate curvature  $R_0/R_c$  for  $\lambda_c = \lambda_w$  and  $v_0 = 0$ . The two varied parameters of the curves are indicated in the legends by color and line style, respectively. Colored symbols show results from lattice-Boltzmann simulations. Inset in (a): master curve  $\langle v_p \rangle/v_m = \sqrt{1 - v_1^2/v_*^2} - 1$  with  $v_* = 2v_m/\mathcal{G}_1$ . In (b), (c) the magnitude  $|\langle v_p \rangle|$  is plotted.

of the function  $\mathcal{G}_1(R_1/R_0)$  (see the Supplementary Material, Sect. II). No matter the phase shift between the wall corrugation and the metachronal wave, the cilia beatings in the fore and aft directions compensate each other. The dip in  $v_p(t)$  arises when the system transitions between two flow morphologies. For  $R_1/R_0$  below  $R_1^*/R_0$ , the velocity field reveals a fluid layer that spans the entire modulated channel and flows in the same direction as the ciliate [blue-shaded region in Fig. 2 (b)]. In the opposite case (e.g.  $R_1/R_0 = 0.8$ ), the size of this layer is greatly reduced, and the flow is dominated instead by large vortices within the pockets. At  $R_1/R_0 = R_1^*/R_0$ , the two flow types cancel each other and  $\langle v_p \rangle$  drops to zero. More details can be found in the Supplementary Material together with illustrative Videos 4-6. Finally, Fig. 3(c) demonstrates that with increasing ciliate curvature  $R_0/R_c$ , the swimming velocity decreases. Thus, ciliates with negligible curvature ( $R_0/R_c \rightarrow 0$ ) swim fastest. The presented curves are directly supported by lattice-Boltzmann simulations, as the symbols in Figs. 3(a)-(c) show.

Now, we relax the condition  $\lambda_c = \lambda_w$  and show in Fig. 4(a) that net swimming is also possible for the higher harmonics,  $\lambda_w/\lambda_c = n$ , as predicted by Eq. (5). The swimming velocity decreases with this ratio once the phase-locked regime with  $v_p/v_m = -1$  is no longer reached.

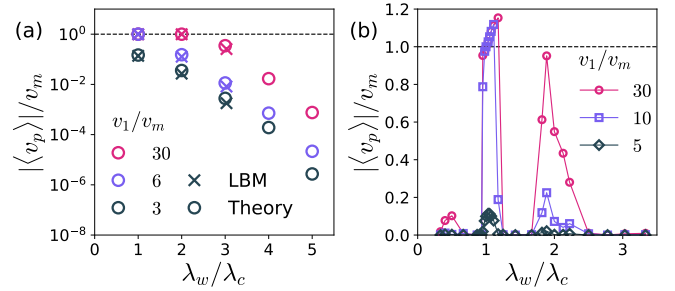


FIG. 4. Time-averaged ciliate velocity  $|\langle v_p \rangle|$  vs. the ratio  $\lambda_w/\lambda_c$  for various  $v_1/v_m$ . (a) Long ciliate with length  $L_c/\lambda_w \gg 1$ . (b) Results from lattice-Boltzmann simulations for a finite ciliate with length  $L_c/\lambda_c = 2.4$  and  $d/L_c = 0.25$ , where  $d$  is the surface-to-surface distance between the finite ciliate and its periodic image. For both panels,  $R_0/R_c = 3/5$ ,  $R_0/\lambda_c = 1/4$ , and  $R_1/R_0 = 1/3$ .

Finally, we relax the limit of a very long ciliate, which allows swimming motion only at the metachronal wavelengths  $\lambda_c = \lambda_w/n$ . To demonstrate the corrugation-enabled motion also for finite ciliates, we perform lattice-Boltzmann simulations for ciliates with length  $L_c/\lambda_c = 2.4$  and shaped like spherocylinders with no-slip boundary conditions on the spherical half-caps (Supplementary Video 3). We again observe oscillatory trajectories with net drift. As expected, peaks in the time-averaged propulsion velocity exist around the integer ratios  $\lambda_w/\lambda_c$  but now they have a finite width [see Fig. 4(b)]. Further interesting features are visible: motion is also possible for  $\lambda_w/\lambda_c < 1$ , a time-averaged speed larger than  $v_m$  occurs, and the peak for  $\lambda_w/\lambda_c = 3$  is suppressed. However, a more thorough investigation of the influence of  $L_c/\lambda_c$  on the propulsion speed is beyond the scope of this Letter.

Using lubrication theory and lattice-Boltzmann simulations, we show that the explicit time dynamics of metachronal waves enables ciliates to swim in a corrugated channel, even if they do not move, on average, in a bulk fluid. This is due to a resonance between the local hydrodynamic resistance, arising from a spatially-varying radius of the channel, and the active flows generated by a sinusoidal metachronal wave. We rationalize our findings via the Adler equation that describes the transition from the oscillatory to the ballistic swimming regime. The mean swimming velocity can even reverse compared to the bulk fluid.

This reversal of direction of motion may be used to fabricate a filter or chromatograph, which blocks the passage of a microorganism with a metachronal wave matching the channel corrugation, but allows other microorganism to pass. In general, our work provides a deeper understanding of how ciliates or any microswimmer with a spatio-temporal fluid forcing at its surface behave in a corrugated channel. As such, it also applies to artificial swimmers and their robotic applications.

## ACKNOWLEDGMENTS

We thank Andrej Vilfan and Paolo Malgaretti for fruitful discussions.

## DATA AVAILABILITY STATEMENT

The data for the current publication will be made available on Zenodo. Upon acceptance of the manuscript the Zenodo repository will be provided.

---

[1] E. M. Purcell, Life at low reynolds number, *Am. J. Phys.* **45**, 3 (1977).

[2] S. Mukherjee and D. B. Kearns, The structure and regulation of flagella in *bacillus subtilis*, *Annu. Rev. Genet.* **48**, 319 (2014).

[3] J. Lin, K. Okada, M. Raytchev, M. C. Smith, and D. Nicastro, Structural mechanism of the dynein power stroke, *Nat. Cell Biol.* **16**, 479 (2014).

[4] E. Lauga, Life around the scallop theorem, *Soft Matter* **7**, 3060 (2011).

[5] M. J. Lighthill, On the squirming motion of nearly spherical deformable bodies through liquids at very small reynolds numbers, *Commun. Pure Appl. Math.* **5**, 109 (1952).

[6] J. R. Blake, A spherical envelope approach to ciliary propulsion, *J. Fluid Mech.* **46**, 199–208 (1971).

[7] T. Ishikawa, Fluid dynamics of squirmers and ciliated microorganisms, *Annu. Rev. Fluid Mech.* **56**, 119 (2024).

[8] N. G. Chisholm, D. Legendre, E. Lauga, and A. S. Khair, A squirmer across reynolds numbers, *J. Fluid Mech.* **796**, 233–256 (2016).

[9] A. W. Zantop and H. Stark, Squirmer rods as elongated microswimmers: flow fields and confinement, *Soft Matter* **16**, 6400 (2020).

[10] S. E. Spagnolie and E. Lauga, Hydrodynamics of self-propulsion near a boundary: predictions and accuracy of far-field approximations, *J. Fluid Mech.* **700**, 105–147 (2012).

[11] E. Lauga and S. Michelin, Stresslets induced by active swimmers, *Phys. Rev. Lett.* **117**, 148001 (2016).

[12] J. M. Yeomans, D. O. Pushkin, and H. Shum, An introduction to the hydrodynamics of swimming microorganisms, *Eur. Phys. J. Special Topics* **223**, 1771 (2014).

[13] K. Drescher, R. E. Goldstein, N. Michel, M. Polin, and I. Tuval, Direct measurement of the flow field around swimming microorganisms, *Phys. Rev. Lett.* **105**, 168101 (2010).

[14] G. S. Klindt and B. M. Friedrich, Flagellar swimmers oscillate between pusher- and puller-type swimming, *Phys. Rev. E* **92**, 063019 (2015).

[15] T. J. Pedley, D. R. Brumley, and R. E. Goldstein, Squirmers with swirl: a model for *volvox* swimming, *J. Fluid Mech.* **798**, 165–186 (2016).

[16] J. S. Guasto, K. A. Johnson, and J. P. Gollub, Oscillatory flows induced by microorganisms swimming in two dimensions, *Phys. Rev. Lett.* **105**, 168102 (2010).

[17] F. Stegemerten, K. John, and U. Thiele, Symmetry-breaking, motion and bistability of active drops through polarization-surface coupling, *Soft Matter* **18**, 5823 (2022).

[18] S. Zheng, D. Carugo, A. Mosayyebi, B. Turney, F. Burkhard, D. Lange, D. Obrist, S. Waters, and F. Clavica, Fluid mechanical modeling of the upper urinary tract, *WIREs Mech Dis.* **13**, e1523 (2021).

[19] P. S. Lykoudis and R. Roos, The fluid mechanics of the ureter from a lubrication theory point of view, *J. Fluid Mech.* **43**, 661–674 (1970).

[20] V. A. Kozlov' and S. A. Nazarov, One-dimensional model of viscoelastic blood flow through a thin elastic vessel, *J. Math. Sci.* **207**, 249 (2015).

[21] D. Dowson, A generalized reynolds equation for fluid-film lubrication, *Int. J. Mech. Sci.* **4**, 159 (1962).

[22] R. Patel, Z. A. Khan, A. Saeed, and V. Bakolas, A review of mixed lubrication modelling and simulation, *Tribology in Industry* **44**, 150 (2022).

[23] R. H. Davis, J.-M. Serayssol, and E. J. Hinch, The elastohydrodynamic collision of two spheres, *J. Fluid Mech.* **163**, 479–497 (1986).

[24] B. Rallabandi, Fluid-elastic interactions near contact at low reynolds number, *Annu. Rev. Fluid Mech.* **56**, 491 (2024).

[25] G. C. Antunes, P. Malgaretti, J. Harting, and S. Dietrich, Pumping and mixing in active pores, *Phys. Rev. Lett.* **129**, 188003 (2022).

[26] G. C. Antunes, P. Malgaretti, and J. Harting, Turning catalytically active pores into active pumps, *J. Chem. Phys.* **159**, 134903 (2023).

[27] G. C. Antunes, M. Jiménez-Sánchez, P. Malgaretti, J. Bachmann, and J. Harting, The interplay of shape and catalyst distribution in the yield of compressible flow microreactors, *J. Chem. Phys.* **161**, 124708 (2024).

[28] T. Richter, P. Malgaretti, T. M. Koller, and J. Harting, Chemically reactive thin films: Dynamics and stability, *Adv. Mater. Interfaces* **12**, 2400835 (2025).

[29] F. Voss and U. Thiele, Gradient dynamics approach to reactive thin-film hydrodynamics, *J. Eng. Math.* **149**, 2 (2024).

[30] S. Bai, P. Huang, Y. Meng, and S. Wen, Modeling and analysis of interfacial electro-kinetic effects on thin film lubrication, *Tribol. Int.* **39**, 1405 (2006).

[31] P. Malgaretti, I. Pagonabarraga, and J. M. Rubi, Entropic electrokinetics: Recirculation, particle separation, and negative mobility, *Phys. Rev. Lett.* **113**, 128301 (2014).

[32] U. Thiele, L. Brusch, M. Bestehorn, and M. Bär, Modelling thin-film dewetting on structured substrates and templates: Bifurcation analysis and numerical simulations, *Eur. Phys. J. E* **11**, 255 (2003).

[33] T. P. Witelski and A. J. Bernoff, Dynamics of three-dimensional thin film rupture, *Physica D* **147**, 155 (2000).

[34] S. Yang, S. Kumar, and C. S. Dutcher, Vertical concentration gradients of soluble surfactants in the rupture of thin liquid films, *J. Colloid Interface Sci.* **687**, 238 (2025).

[35] V. Charitatos and S. Kumar, A thin-film model for droplet spreading on soft solid substrates, *Soft Matter* **16**, 8284 (2020).

- [36] S. Jana, S. H. Um, and S. Jung, Paramecium swimming in capillary tube, *Phys. Fluids* **24**, 041901 (2012).
- [37] J. Gray, The mechanism of ciliary movement, *Proc. R. Soc. London, Ser. B* **93**, 104 (1922).
- [38] D. R. Brumley, M. Polin, T. J. Pedley, and R. E. Goldstein, Hydrodynamic synchronization and metachronal waves on the surface of the colonial alga *volvox carteri*, *Phys. Rev. Lett.* **109**, 268102 (2012).
- [39] B. Guirao and J.-F. Joanny, Spontaneous creation of macroscopic flow and metachronal waves in an array of cilia, *Biophys. J.* **92**, 1900 (2007).
- [40] R. N. Poon, T. A. Westwood, H. Laeverenz-Schlogelhofer, E. Brodrick, J. Craggs, E. E. Keaveny, G. Jékely, and K. Y. Wan, Ciliary propulsion and metachronal coordination in reef coral larvae, *Phys. Rev. Res.* **5**, L042037 (2023).
- [41] J. Elgeti and G. Gompper, Emergence of metachronal waves in cilia arrays, *PNAS* **110**, 4470 (2013).
- [42] S. N. Khaderi, J. M. J. den Toonder, and P. R. Onck, Fluid flow due to collective non-reciprocal motion of symmetrically-beating artificial cilia, *Biomicrofluidics* **6**, 014106 (2012).
- [43] H. Schlichting, *Boundary Layer Theory* (McGraw-Hill, New York, 1979).
- [44] S. Strogatz, *Nonlinear Dynamics and Chaos* (CRC Press, Boca Raton, 2015).
- [45] R. Adler, A study of locking phenomena in oscillators, *Proc. IRE* **34**, 351 (1946).
- [46] J. Grawitter and H. Stark, Steering droplets on substrates with plane-wave wettability patterns and deformations, *Soft Matter* **20**, 3161 (2024).
- [47] A. Funfak, C. Fisch, H. T. Abdel Motaal, J. Diener, L. Combettes, C. N. Baroud, and P. Dupuis-Williams, Paramecium swimming and ciliary beating patterns: a study on four rna interference mutations, *Integr. Biol.* **7**, 90 (2014).
- [48] S. L. Tamm and G. A. Horridge, The relation between the orientation of the central fibrils and the direction of beat in cilia of opalina, *Proc. R. Soc. London, Ser. B* **175**, 219 (1970).
- [49] T. Krüger, H. Kusumaatmaja, A. Kuzmin, O. Shardt, G. Silva, and E. Viggen, *The Lattice Boltzmann Method* (Springer, Berlin, 2017).

## SUPPLEMENTARY MATERIAL

### I. LUBRICATION THEORY

In this section, we solve the problem of a long ciliate swimming in a corrugated cylindrical channel in the lubrication approximation regime. In this regime, characteristic lengths ruling the dynamics along the channel in the  $x$ -direction ( $\lambda_c, \lambda_w$ ) are much larger than the ones ruling the dynamics in the radial  $r$ -direction ( $R_0, R_1$ ). We refer to Fig. 1(a) in the main text for the definition of all the lengths. We now define the dimensionless quantities

$$\hat{x} = \frac{x}{\bar{\lambda}}, \text{ and } \hat{r} = \frac{r}{R_0}, \quad (\text{S1})$$

where  $\bar{\lambda}$  is the smallest longitudinal characteristic length

$$\bar{\lambda} = \min(\lambda_c, \lambda_w). \quad (\text{S2})$$

Note that because  $R(x)$  is greater than zero, we have  $R_0 > R_1$ , and so  $R_0$  is the largest transversal characteristic length. In cylindrical coordinates the  $x$ -component of the Laplacian of the velocity vector in the Stokes equations can then be written as

$$(\Delta \mathbf{v}) \cdot \mathbf{e}_x = \frac{1}{R_0^2} \frac{1}{\hat{r}} \partial_{\hat{r}} (\hat{r} \partial_{\hat{r}} v_x) + \frac{1}{\bar{\lambda}^2} \partial_{\hat{x}}^2 v_x. \quad (\text{S3})$$

Derivatives of  $v_x$  with respect to the hatted coordinates will be quantities of the same magnitude as the latter are all quantities normalized by their characteristic magnitudes. As such, the second term on the right-hand-side of Eq. (S3) is by a factor  $(R_0/\bar{\lambda})^2$  smaller than the first term. Provided that  $R_0/\bar{\lambda} \ll 1$ , we may thus write

$$(\Delta \mathbf{v}) \cdot \mathbf{e}_x \approx \frac{1}{r} \partial_r (r \partial_r v_x). \quad (\text{S4})$$

In a similar way, one can prove that the variation of pressure in the transversal direction is also by a factor  $(R_0/\bar{\lambda})^2$  smaller than in the longitudinal direction [26], so that one ultimately has  $v_r \ll v_x$ . As such, the relevant Stokes equation (governing fluid flow at small Reynolds numbers) yields

$$\partial_x P(x, t) = \mu \frac{1}{r} \partial_r [r \partial_r v_x(x, r, t)], \quad (\text{S5})$$

where  $\mu$  is the shear viscosity and where we have made use of the radial symmetry of the problem.

Equation (S5) can be integrated twice in the radial direction, yielding

$$v_x(x, r, t) = -\frac{\partial_x P(x, t)}{4\mu} \left[ R^2(x) - r^2 - \frac{\log\left(\frac{R(x)}{R_0}\right)}{\log\left(\frac{R(x)}{R_c}\right)} [R^2(x) - R_c^2] \right] + \frac{\log\left(\frac{R(x)}{r}\right)}{\log\left(\frac{R(x)}{R_c}\right)} [v_p(t) + v_c(x, t)], \quad (\text{S6})$$

when using the boundary conditions in Eqs. (2) and  $v_x(x, r = R(x), t) = 0$ , as formulated in the main text.

The second term of the right-hand side of Eq. (S6) is proportional to the slip velocity imposed by the ciliary beating and encodes the active driving of the fluid. The first term on the right-hand side is a Poiseuille-like term that is proportional to a local pressure gradient with a local hydrodynamic resistance, which depends on the thickness of the fluid film. This term is a passive contribution coming from locally-generated pressure gradients that are required to enforce incompressibility,  $\nabla \cdot \mathbf{v}(\mathbf{r}, t) = 0$ . Indeed, incompressibility implies that the flow rate  $Q(t)$  across every cross-section of the film,

$$Q(t) = 2\pi \int_{R_c}^{R(x)} r v_x(x, r, t) dr, \quad (\text{S7})$$

be homogeneous in space, so it does not depend on  $x$ . Plugging in the velocity field from Eq. (S6) yields

$$Q(t) = f_1(x) \partial_x P(x, t) + f_2(x) [v_p(t) + v_c(x, t)], \quad (\text{S8})$$

where

$$f_1(x) = -\frac{\pi}{8\mu} \left\{ \left( 1 - \frac{1}{\log\left(\frac{R(x)}{R_c}\right)} \right) [R^2(x) - R_c^2]^2 + 2R_c^2[R^2(x) - R_c^2] \right\} \quad (\text{S9})$$

and

$$f_2(x) = 2\pi \left[ \frac{R^2(x) - R_c^2}{4\log\left(\frac{R(x)}{R_c}\right)} - \frac{R_c^2}{2} \right] \quad (\text{S10})$$

are auxiliary functions of position only, which can be computed as both  $R_c$  and  $R(x)$  are known parameters of the system. Isolating the pressure gradient in Eq. (S8) yields

$$\partial_x P(x, t) = \frac{Q(t) - f_2(x)[v_p(t) + v_c(x, t)]}{f_1(x)}, \quad (\text{S11})$$

which we average now over the entire domain. To do so, we integrate over the domain  $x \in [-L, L]$  where  $L$  is a generic length and divide the result by  $2L$ . We then take the limit  $L \rightarrow \infty$ . From here on, we denote this operation on a generic function  $g(x)$  with angular brackets such that

$$\langle g(x) \rangle \equiv \lim_{L \rightarrow \infty} \frac{1}{2L} \int_{-L}^L g(x) dx. \quad (\text{S12})$$

Averaging Eq. (S11) and using the fact that there is no externally-imposed pressure gradient,

$$\lim_{L \rightarrow \infty} \frac{P(x = L, r, t) - P(x = -L, r, t)}{2L} = 0, \quad (\text{S13})$$

yields

$$Q(t) = \frac{\langle \frac{f_2(x)}{f_1(x)} [v_p(t) + v_c(x, t)] \rangle}{\langle f_1^{-1}(x) \rangle}, \quad (\text{S14})$$

where we have used Eq. (S13). The flux  $Q(t)$  cannot yet be computed as we do not know  $v_p(t)$ . We solve this issue by using the force-free condition,  $\oint_S \boldsymbol{\sigma}(\mathbf{r}, t) \cdot \mathbf{n}(\mathbf{r}, t) dS = \mathbf{0}$ . The force per unit length  $f_x(L)$  that the fluid exerts on the ciliate in the domain  $x \in [-L, L]$  is

$$f_x(L) = \frac{2\pi R_c}{2L} \int_{-L}^L \sigma_{x,r}(x, r = R_c, t) dx \quad (\text{S15})$$

where  $\sigma_{x,r}(x, r = R_c, t)$  is

$$\sigma_{x,r}(x, r, t) = \mu[\partial_x v_r(x, r = R_c, t) + \partial_r v_x(x, r = R_c, t)]. \quad (\text{S16})$$

The first term in the right-hand side is zero due to the boundary condition in Eq. (2) in the main text. Because the motion is force-free, the total force on the ciliate is zero, and thus so is the force per unit length

$$\lim_{L \rightarrow \infty} f_x(L) = 0. \quad (\text{S17})$$

Plugging in the velocity field of Eq. (S6) in Eq. (S15) and taking the limit of  $L \rightarrow \infty$  yields

$$\langle \alpha(x) \partial_x P(x, t) \rangle = -\langle \beta(x) [v_p + v_c(x, t)] \rangle, \quad (\text{S18})$$

where

$$\alpha(x) = \frac{R_c}{2\mu} - \frac{R^2(x) - R_c^2}{4\mu R_c \log\left(\frac{R(x)}{R_c}\right)} \quad (\text{S19})$$

and

$$\beta(x) = -\frac{1}{R_c \log\left(\frac{R(x)}{R_c}\right)} \quad (S20)$$

are auxiliary functions which like  $f_1(x)$  and  $f_2(x)$  depend only on position and are computable. Plugging the pressure gradient from Eq. (S11) with the flow rate from Eq. (S14) into Eq. (S18) yields

$$\begin{aligned} -\langle \beta(x)[v_p(t) + v_c(x, t)] \rangle &= \langle f_2(x)f_1^{-1}(x)[v_p(t) + v_c(x, t)] \rangle \langle f_1^{-1}(x) \rangle^{-1} \langle \alpha(x)f_1^{-1}(x) \rangle \\ &\quad - \langle \alpha(x)f_2(x)f_1^{-1}(x)[v_p(t) + v_c(x, t)] \rangle. \end{aligned} \quad (S21)$$

Since  $v_p(t)$  does not depend on the coordinate  $x$ , we may isolate it to obtain

$$v_p(t) = \dot{x}_p(t) = -\frac{\langle \beta(x)v_c(x, t) \rangle + \langle f_2(x)f_1^{-1}(x)v_c(x, t) \rangle \langle f_1^{-1}(x) \rangle^{-1} \langle \alpha(x)f_1^{-1}(x) \rangle - \langle \alpha(x)f_2(x)f_1^{-1}(x)v_c(x, t) \rangle}{\langle \beta(x) \rangle + \langle f_2(x)f_1^{-1}(x) \rangle \langle f_1^{-1}(x) \rangle^{-1} \langle \alpha(x)f_1^{-1}(x) \rangle - \langle \alpha(x)f_2(x)f_1^{-1}(x) \rangle}, \quad (S22)$$

which is finally computable as all variables on the right-hand side are known.

For further clarity, we write Eq. (S22) as

$$v_p(t) = -\langle \mathcal{G}(x)v_c(x, t) \rangle, \quad (S23)$$

which is a weighted average of  $v_c(x, t)$ , with a weight

$$\mathcal{G}(x) = \frac{\beta + f_2f_1^{-1}\langle f_1^{-1} \rangle^{-1}\langle \alpha f_1^{-1} \rangle - \alpha f_2f_1^{-1}}{\langle \beta \rangle + \langle f_2f_1^{-1} \rangle \langle f_1^{-1} \rangle^{-1}\langle \alpha f_1^{-1} \rangle - \langle \alpha f_2f_1^{-1} \rangle}, \quad (S24)$$

where we have omitted the function arguments on the right-hand side for improved readability.

We have now reduced the full 3D hydrodynamics problem to an ordinary differential equation of the form  $\dot{x}_p = \mathcal{F}(x_p, t)$ , which can easily be solved numerically. Such procedure was done to generate the data in Figs. 3 and 4. Because we choose  $R(x)$  to be a  $\lambda_w$ -periodic function, so is  $\mathcal{G}(x)$ , and so we may write

$$\mathcal{G}(x) = \sum_{m=0}^{\infty} \mathcal{G}_m \cos\left(\frac{2\pi}{\lambda_c}mx\right) + \tilde{\mathcal{G}}_m \sin\left(\frac{2\pi}{\lambda_c}mx\right), \quad (S25)$$

where  $\mathcal{G}_m$  and  $\tilde{\mathcal{G}}_m$  are the  $m$ -th Fourier coefficients

$$\mathcal{G}_m = \frac{2}{\lambda_w} \int_0^{\lambda_w} \mathcal{G}(x) \cos\left(\frac{2\pi}{\lambda_w}m\right) dx, \quad (S26)$$

and

$$\tilde{\mathcal{G}}_m = \frac{2}{\lambda_w} \int_0^{\lambda_w} \mathcal{G}(x) \sin\left(\frac{2\pi}{\lambda_w}m\right) dx. \quad (S27)$$

Plugging in the sinusoidal form of Eq. (3) and Eq. (S25) into Eq. (S23) yields

$$v_p(t) = -v_0 - v_1 \frac{\mathcal{G}_n}{2} \cos[k_c x_p(t) + \omega t], \quad (S28)$$

where  $\mathcal{G}_n$  is the Fourier coefficient whose index  $n$  corresponds to the metachronal wavelength such that  $\lambda_w/n = \lambda_c$ . As described in the main text, this equation is reducible to the Adler equation, for which the time-averaged velocity and the period of motion can be computed analytically. Nonetheless, calculating the coefficient  $\mathcal{G}_n$  analytically presents a formidable challenge in the general case. Analytical progress can be made in the limits of thin fluid films ( $R_0/R_c \ll 1$ ) and shallow corrugation ( $R_1/R_0 \ll 1$ ). In such a limit, one may expand  $\mathcal{G}(x)$  to linear order in both of these dimensionless numbers and obtain  $\mathcal{G}_1 = 2R_1/R_0$  as the only non-zero Fourier coefficient in this limit, as stated in the main text.

In particular, since the Fourier series of  $\mathcal{G}(x)$  does not contain terms corresponding to wavelengths  $\lambda_c > \lambda_w$ , no motion is attained in this region of parameter space, as stated in the main text and seen in Fig. 4(a). In fact, the Fourier series will only contain a term of wavelength  $\lambda_c$  if  $\lambda_w$  is indeed a multiple of  $\lambda_c$ , again as discussed in the main text.

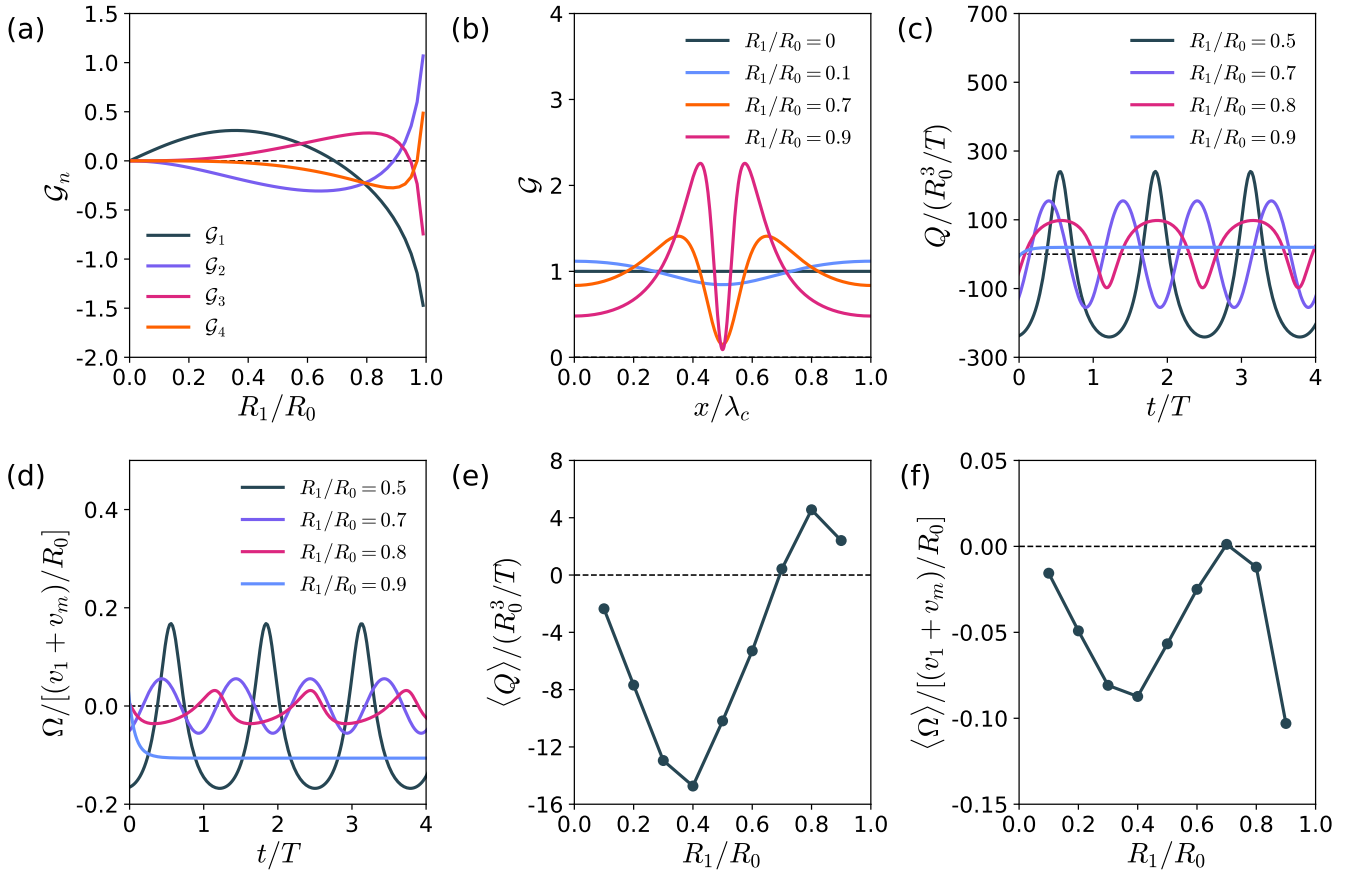


FIG. S1. (a) Fourier components  $\mathcal{G}_n$  as a function of corrugation amplitude  $R_1/R_0$  for various  $n$ . (b) Mobility function  $\mathcal{G}(x)$  as a function of position  $x/\lambda_c$  for various  $R_1/R_0$ . (c) Flow rate  $Q$  and (d) vorticity  $\Omega$  as a function of time for various  $R_1/R_0$ . (e) Time-averaged flow rate  $\langle Q \rangle$  and (f) vorticity  $\langle \Omega \rangle$  as a function of  $R_1/R_0$ . For all panels,  $R_0/R_c = 1$ ,  $v_1/v_m = 5$ ,  $v_0 = 0$ ,  $\lambda_c/\lambda_w = 1$ .

## II. FLOW MORPHOLOGY WITH CHANGING $R_1/R_0$

The time-averaged velocity (when  $v_0 = 0$  and  $\lambda_w = \lambda_c$ ) was shown in the main text in Fig. 3(b) to have a local minimum upon a change of corrugation amplitude  $R_1/R_0$  at a value  $R_1^*/R_0 \approx 0.6 - 0.7$ . An analysis of the trajectories reveals that not only the time-averaged velocity is zero, but so is the instantaneous velocity. According to Eq. (4), such can only occur if  $\mathcal{G}_1 = 0$ . For brevity, we focus on the case  $R_0/R_c = 1$ ,  $v_1/v_m = 5$ , and show in Fig. S1(a) that  $\mathcal{G}_1(R_1/R_0)$  indeed displays a root at  $R_1^*/R_0 \approx 0.7$ . Note that flipping the sign of  $\mathcal{G}_1$  results in the same value of  $\langle v_p \rangle$ , as the factor  $-1$  may be absorbed in Eq. (6) by shifting the phase  $\xi$  by  $\pi$ . For further clarity, we plot the mobility function  $\mathcal{G}(x)$  for varying values of  $R_1/R_0$  in Fig. S1(b). In order to shed further light on the mechanism underlying the dip in velocity, we examine the morphology of the velocity field, which we quantify via two quantities: the total flow rate  $Q(t)$  across the channel,

$$Q(t) = 2\pi \int_{R_c}^{R(x)} r v_x(x, r, t) dr, \quad (S29)$$

which due to incompressibility, is independent of the value of  $x$  for which it is calculated; and the total vorticity averaged over the volume enclosed by the cylinder and one period of the corrugated by wall

$$\Omega(t) = \frac{2\pi}{V} \int_0^{\lambda_w} \int_{R_c}^{R(x)} [\partial_x v_r(x, r, t) - \partial_r v_x(x, r, t)] r dr dx, \quad (S30)$$

where  $V$  is the volume

$$V = 2\pi \int_0^{\lambda_w} \int_{R_c}^{R(x)} r dr dx. \quad (\text{S31})$$

In Figs. S1(c) and (d), it can be seen that both quantities either oscillate in time or tend to a steady state, depending on whether the motion is in the oscillatory or phase-locked regime. The time-averaged values of these quantities are non-zero, in general, as can be seen in Figs. S1(e) and (f). The value of  $R_1/R_0$ , where both vorticity and flow rate vanish, coincides with  $R_1^*/R_0$ . Corrugations sufficiently shallower than  $R_1^*/R_0$  (e.g.  $R_1/R_0 = 0.5$ ) showcase large absolute values of  $Q(t)$ , which result from a layer in which fluid moves along the entire channel. When crossing  $R_1^*/R_0$ ,  $Q(t)$  flips sign but attains values much smaller than in the previous case. The vorticity displays the inverse trend, and attains its largest value when  $R_1/R_0 > R_1^*/R_0$ . The channel-spanning layer becomes then much thinner, and the velocity field is dominated by vortices localized between successive bottlenecks (see also Supplementary Videos 4-6). Motion via the first morphology requires the channel-spanning layer of fluid to travel in the same direction as the ciliate ( $\langle Q \rangle < 0$ ), forcing the vortices near the ciliate to rotate counterclockwise (against the ciliate motion). The second morphology requires the latter to rotate clockwise (with the ciliate motion), forcing the channel-spanning layer to flow in the opposite direction ( $\langle Q \rangle > 0$ , against the ciliate motion). The dip then arises when none of these two flow morphologies dominates. Instead, they counteract each other and the ciliate stops moving.

### III. SUPPLEMENTARY VIDEOS

There are six videos supplied with this manuscript:

- Supplementary Video 1 depicts motion in the oscillatory regime, as obtained by the theory of section I. Pictured is half of the cross-section of the corrugated channel along the longitudinal and radial direction. Black arrows point in the direction of the velocity field and blue/red colors indicate the velocity component  $v_x$  in the longitudinal direction. The black area on top corresponds to the channel wall, and the green area to the ciliary body. An eye fixed to the ciliary body has been added. The center of this eye corresponds to the variable  $x_p(t)$  and as such shows the motion of the ciliate. Parameters:  $v_0 = 0$ ,  $R_0/R_c = 3/5$ ,  $R_1/R_0 = 1/3$ ,  $R_0/\lambda_c = 3/20$ ,  $\lambda_c/\lambda_w = 1$ ,  $v_1/v_m = 3.6$ .
- Supplementary Video 2 depicts motion in the phase-locked regime regime, as obtained by the theory of section I. Color coding as per Supplementary Video 1. Parameters:  $v_0 = 0$ ,  $R_0/R_c = 3/5$ ,  $R_1/R_0 = 1/3$ ,  $R_0/\lambda_c = 3/20$ ,  $\lambda_c/\lambda_w = 1$ ,  $v_1/v_m = 7.5$ .
- Supplementary Video 3 depicts the motion of a finite ciliate as obtained by lattice-Boltzmann simulations. The ciliate is shaped like a spherocylinder with radius  $R_c$  and length  $L_c$  (including the hemispherical ends). The slip velocity is only applied on the surface of the cylinder part of the ciliate. In the hemispherical ends, no slip boundary conditions are applied. Color coding as per Supplementary Video 1. Dashed black line marks the eye's starting position. Parameters:  $v_0 = 0$ ,  $R_0/R_c = 3/5$ ,  $R_1/R_0 = 1/3$ ,  $\lambda_c/\lambda_w = 1$ ,  $R_0/\lambda_w = 1$ ,  $v_1/v_m = 12$ ,  $L_c/\lambda_c = 12.4$ .
- Supplementary Video 4 depicts a ciliate confined to a channel whose value of  $R_1/R_0$  is lower than  $R_1^*/R_0$ , where the dip in Fig. 3(b) occurs. Color coding as per Supplementary Video 1. Parameters are  $R_1/R_0 = 0.5$ ,  $v_1/v_m = 5$ ,  $v_0 = 0$ ,  $R_0/R_c = 1$ ,  $R_0/\lambda_w = 1/4$ ,  $\lambda_w/\lambda_c = 1$ .
- Supplementary Video 5 depicts a ciliate confined to a channel whose value of  $R_1/R_0$  is approximately that of  $R_1^*/R_0$ , where the dip in Fig. 3(b) occurs. Color coding as per Supplementary Video 1. Parameters are  $R_1/R_0 = 0.7$ ,  $v_1/v_m = 5$ ,  $v_0 = 0$ ,  $R_0/R_c = 1$ ,  $R_0/\lambda_w = 1/4$ ,  $\lambda_w/\lambda_c = 1$ .
- Supplementary Video 6 depicts a ciliate confined to a channel whose value of  $R_1/R_0$  is greater than  $R_1^*/R_0$ , where the dip in Fig. 3(b) occurs. Color coding as per Supplementary Video 1. Parameters are  $R_1/R_0 = 0.8$ ,  $v_1/v_m = 5$ ,  $v_0 = 0$ ,  $R_0/R_c = 1$ ,  $R_0/\lambda_w = 1/4$ ,  $\lambda_w/\lambda_c = 1$ .